

The Finite Volume Method in Computational Rheology

A.M. Afonso¹, M.S.N. Oliveira¹, P.J. Oliveira², M.A. Alves¹ and F.T. Pinho¹

¹*Transport Phenomena Research Centre, Faculty of Engineering
University of Porto, Porto*

²*Department of Electromechanical Engineering, Textile and Paper Materials Unit
University of Beira Interior, Covilhã
Portugal*

1. Introduction

The finite volume method (FVM) is widely used in traditional computational fluid dynamics (CFD), and many commercial CFD codes are based on this technique which is typically less demanding in computational resources than finite element methods (FEM). However, for historical reasons, a large number of Computational Rheology codes are based on FEM.

There is no clear reason why the FVM should not be as successful as finite element based techniques in Computational Rheology and its applications, such as polymer processing or, more recently, microfluidic systems using complex fluids. This chapter describes the major advances on this topic since its inception in the early 1990's, and is organized as follows. In the next section, a review of the major contributions to computational rheology using finite volume techniques is carried out, followed by a detailed explanation of the methodology developed by the authors. This section includes recent developments and methodologies related to the description of the viscoelastic constitutive equations used to alleviate the high-Weissenberg number problem, such as the log-conformation formulation and the recent kernel-conformation technique. At the end, results of numerical calculations are presented for the well-known benchmark flow in a 4:1 planar contraction to ascertain the quality of the predictions by this method.

2. Main contributions

The first contributions to computational rheology in the late nineteen sixties were based on finite difference methods (FDM, Perera and Walters, 1977). In the first major book on computational rheology (Crochet et al, 1984) works using FEM predominate, but the number of contributions using FDM was also significant.

Among the first numerical works to make use of FVM to investigate viscoelastic fluid flows was the study of the benchmark flow around a confined cylinder of Hu and Joseph (1990), who used the simplest differential constitutive equation embodying elastic effects, the upper-convected Maxwell (UCM) model. Velocities were calculated in cylindrical/orthogonal grids

staggered relative to the basic mesh for pressure and stresses. The SIMPLER algorithm (Patankar, 1980) was adapted and extended to the calculation of stress tensor components. The inertial terms in the momentum equation were neglected in these low Reynolds number simulations conducted on rather coarse meshes, and convergence was obtained up to Weissenberg numbers of 10.

For creeping flow, the advective terms in the momentum equation can be discarded but the same does not hold for the advective terms in the constitutive equation, which typically originate convergence and accuracy problems. The development of stable and accurate schemes to deal with advection-dominated equations is a fundamental issue which was not addressed in the initial works using FVM. For example, in their sudden contraction calculations Yoo and Na (1991) kept all advective terms, but considered only first order discretization schemes, which are known from classical CFD (Leschziner, 1980) to introduce excessive numerical diffusion, especially when the flow is not aligned with the computational grid (Patankar, 1980).

Staggered meshes, in which different variables are evaluated in different points of the computational mesh (some at the cell centers, others at the cell faces), were used by Yoo and Na (1990), as well as in subsequent works (eg. Gervang and Larsen, 1991; Sasmal, 1995; Xue et al, 1995, 1998 a,b; Mompeam and Deville, 1997; Bevis et al, 1992). Staggered meshes provide an easy way to couple velocities, pressure and stresses, but calculations involving complex geometries become rather difficult and in some cases do not allow for the determination of the shear stress at singular points, such as re-entrant corners. Alternatively, the use of non-orthogonal, or even non-structured meshes, are to be preferred in such cases.

Non-orthogonal meshes have been used in FVM for Newtonian fluids since the mid-nineteen eighties, but its application to finite volume viscoelastic methods happened only in 1995. Initially, the adaptation to computational rheology of some of the techniques previously developed for Newtonian fluids to has been slow, namely on issues like pressure-velocity coupling for collocated meshes (in which all variables are evaluated at the cell centres), time marching algorithms or the use of non-orthogonal meshes. Lately, progress has been quicker on issues of stability for convection dominated flows, as in viscoelastic flows at high Weissenberg numbers and in high speed flows of inviscid Newtonian fluids involving shock waves (Morton and Paisley, 1989; Mackenzie et al, 1993).

Regarding other mesh arrangements, Huang et al (1996) used non-structured methods in a mixed finite element/finite volume formulation by extending the control volume finite element method (CVFEM) of Baliga and Patankar (1983) for the prediction of the journal bearing flow of Phan-Thien and Tanner (PTT) fluids. Nevertheless, the formulation lacked the generality of modern methods in Newtonian fluid calculations on collocated grids (Ferziger and Perić, 2002) and was problematic to extend to higher-order shape functions (usually the convective terms are discretized with some form of upwind). Later, Oliveira et al (1998) developed a general method for solving the full momentum and constitutive equations on collocated non-orthogonal meshes, enabling calculations of complex three-dimensional flows. Their scheme for coupling velocity, pressure and stresses was later improved by Oliveira and Pinho (1999a) and Matos et al (2009). This issue was also addressed in a parallel effort by Missirlis et al (1998), but only for staggered, orthogonal meshes.

As mentioned above, there are hybrid methods, aimed at combining the advantage of finite elements in representing complex geometries and the advantage of finite volumes to ensure

conservation of physical quantities; they follow the CVFEM ideas initially proposed by Baliga and Patankar (1983). Within the scope of computational rheology, hybrid methods have been developed especially by Webster and co-workers (Aboubacar and Webster 2001, Aboubacar et al 2002, Wapperom and Webster 1998, 1999), and Sato and Richardson (1994) within the finite-element methodology; and by Phan-Thien and Dou (1999) and Dou and Phan-Thien (1999), within the CVFEM formulation referred to above.

Stability, convergence and accuracy are intimately related, but the early efforts were more concerned with stability and convergence, due to the mixed elliptic/hyperbolic nature of the motion and constitutive equations, than with accuracy. Thus, early developments on the algorithmic side were usually based on first-order discretization methods, such as the classical upwind differencing scheme, leading to lower accuracy (Ferziger and Perić, 2002). Due to computer limitations early works also used rather coarse meshes, but the topic of accuracy started to gain momentum by the mid-nineties, and Sato and Richardson (1994) were among the first to show this concern. Although their approach can be classified as FEM, the constitutive equations were integrated over finite volumes with the advective flux stress terms discretized and stabilized by means of a bounded scheme obeying total variation diminishing (TVD) criteria.

For the pure FVM in computational rheology, there has been a significant effort at developing accurate and stable methods by the authors of this chapter: Oliveira and Pinho (1999b), Alves et al (2000, 2001a, 2003a, 2003b) and Afonso et al (2009, 2012). Oliveira and Pinho (1999b) used second-order interpolation schemes for the advective stress fluxes (either a linear upwind scheme or central differences), but difficulties associated with the intrinsic unboundedness of those schemes led them to the implementation of so-called high-resolution methods, often used in high-speed aerodynamics. These represent important landmark developments, where there was a remarkable improvement both in terms of stability and accuracy (Alves et al, 2000). In fact, high-resolution methods led to solutions having similar accuracy as those obtained with the most advanced FEM (Alves et al, 2001a, 2003b), and also to comparable levels of convergence (measured by the maximum Weissenberg (Wi) or Deborah (De) numbers above which the methods diverged). For reasons discussed in Fan et al (1999), the lower De results showed less discrepancies and FVM could achieve the same accuracy as FEM. Comparisons for the flow in a 4:1 sudden planar contraction are also available in Alves et al (2003b), where the CUBISTA high-resolution scheme especially designed for the treatment of advection in viscoelastic flows is employed (Alves et al, 2003a). Some of the difficulties in iterative convergence of viscoelastic flow calculations of the mid-2000's were solved by such high-resolution schemes for interpolating convective terms in the stress equation as the CUBISTA scheme, which obeys total variation diminishing criteria. These are more restrictive than convection boundedness criteria and the universal limiter of Leonard (1991), as was demonstrated by Alves et al (2003a).

Subsequently, a very relevant development in computational rheology overcame, or at least significantly mitigated, the so-called High-Weissenberg Number Problem, in which calculations breakdown at some critical problem-dependent Weissenberg numbers. In 2004, Fattal and Kupferman proposed a reformulation of the viscoelastic constitutive equations in terms of the matrix logarithm of the conformation tensor to alleviate this problem (Fattal and Kupferman, 2004). This technique, now known as the log-

conformation, has been implemented within the framework of FEM (eg. Hulsen et al, 2005) and more recently in the framework of FVM (Afonso et al, 2009, 2011), who maintained the use of the CUBISTA scheme to describe the advection of log-conformation terms for improved accuracy. This technique has been applied to various different flows, including the flow around a cylinder, in which Wi on the order of 10 were achieved for the Oldroyd-B model in comparison with previous $Wi \approx 1.2$ attained with the standard version. This approach has been generalized by Afonso et al (2012) considering different functions for the transformation of the tensor evolution equation. This technique, known as kernel-conformation, encompasses the log-conformation approach and assumes particular importance as new phenomena are observed in viscoelastic fluid flows in the context of microfluidics, where elastic effects are enhanced and inertia effects reduced as compared to classical macro-scale fluid flows.

Today it is an undisputable fact that FVM are mature in computational rheology, as indicated by a wide range of computations exhibiting similar or even better performance in terms of accuracy and robustness as other methods (Owens and Phillips, 2002) and presumably at a lower cost, especially in light of the recent developments allowing computations at high Wi number.

3. The finite-volume method applied to viscoelastic fluids using collocated meshes

3.1 General methodology

The general finite-volume methodology here described for viscoelastic flow computations is closely patterned along the lines of that previously presented in Oliveira (1992). Numerical calculation of any flow requires solution of two governing equations, for mass conservation and momentum. For a non-Newtonian fluid an additional rheological equation of state is needed. To calculate the pressure it is necessary to solve a thermodynamic equation of state, but since here we are considering incompressible fluid flows only, such equation is used to calculate the fluid density and becomes decoupled from the above mentioned governing equations. Then the flow becomes independent of absolute pressure, and the pressure variations are determined indirectly from the mass conservation equation as discussed later. If temperature variations are important, the energy equation needs also to be considered.

In FVM, described in detail in several textbooks (eg. Patankar, 1980; Ferziger and Perić, 2002; Versteeg and Malalasekera, 2007), the computational domain is divided into contiguous computational cells and within each of these the differential governing equations are volume integrated. Gauss theorem is then invoked to transform the divergence of quantities into surface integral of fluxes in order to guarantee the conservation of the quantities. Next, these surface integrals are represented by summation of fluxes whereas the non-transformed volume integrals are approximated by products of an average value of the integrand and the volume of the computational cells. Finally, the fluxes at the cell faces must be equated as a function of the unknown quantities at the neighbour cell centers. This is achieved differently depending on whether staggered or collocated meshes are used. For the former see Patankar (1980) and for the latter details are given in Ferziger and Perić (2002). The present chapter deals with collocated meshes only.

3.2 Coordinate system

The equations to be solved are written for non-orthogonal coordinate systems aligned with the computational grid for generality in the treatment of complex geometries. This can also be achieved with non-structured meshes (for viscoelastic fluids, see e.g. Huang et al, 1996), but our developments are based on block-structured grids. The equations must obey general principles of invariance, but their discretization in a global mesh composed of six-faced computational cells requires their previous transformation to a non-orthogonal coordinate system (ξ_1, ξ_2, ξ_3) , as in Figure 1. It is important to notice that only the coordinates are represented in the non-orthogonal system, whereas velocity and stress components are referred to the original Cartesian system. This means that in the transformation of the conservation equations only the derivatives need to be converted.

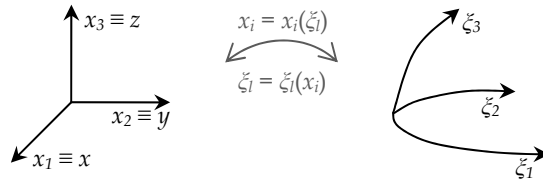


Fig. 1. Schematic representation of the transformation of Cartesian rectangular coordinates to a non-orthogonal system defined by the local orientation of the computational grid.

From the numerical point of view it is advantageous to write the resulting equations in their strong conservative form to help conserve the physical quantities in the final algebraic equations. This is indeed one of the main advantages of FVM: it is essential to maintain conservation of quantities that physically should be conserved, such as mass. The well known transformation rules (see Vinokur, 1989) are given by:

$$\frac{\partial}{\partial t} = \frac{1}{J} \frac{\partial}{\partial t} J$$

$$\frac{\partial}{\partial x_i} = \frac{\partial}{\partial \xi_l} \frac{\partial \xi_l}{\partial x_i} = \frac{1}{J} \frac{\partial}{\partial \xi_l} \beta_{li} = \frac{\beta_{li}}{J} \frac{\partial}{\partial \xi_l} \tag{1}$$

where J is the Jacobian of the transformation $x_i = x_i(\xi_l)$, i.e. $J = \det(\partial x_i / \partial \xi_l)$ and β_{li} are the metric coefficients defined as the cofactor of terms $\partial x_i / \partial \xi_l$ in the Jacobian. These equations are written in terms of indicial notation and the summation convention for repeated indices applies.

3.3 Governing equations

The continuity equation for incompressible fluid flow is

$$\frac{\partial(\rho u_i)}{\partial x_i} = 0 \tag{2}$$

where u_i represents the velocity vector in the Cartesian system and ρ is the density of the fluid, which is retained in Eq. (2) for later convenience. The momentum equation for a generic fluid is given by

$$\frac{\partial \rho u_i}{\partial t} + \frac{\partial \rho u_j u_i}{\partial x_j} = -\frac{\partial p}{\partial x_i} + \rho g_i + \frac{\partial}{\partial x_j} \left(\eta_s \left(\frac{\partial u_i}{\partial x_j} + \frac{\partial u_j}{\partial x_i} \right) \right) + \frac{\partial \tau_{ij}}{\partial x_j} \quad (3)$$

where t represents the time, p the pressure, g_i is the acceleration of gravity, η_s is the solvent viscosity and τ_{ik} is the symmetric extra-stress tensor, which is described by an appropriate rheological constitutive equation. To describe the numerical method, we will adopt the PTT model, which is adequate to explain the variations relative to the method used for Newtonian fluids. Whenever needed the use of a different model will be conveniently mentioned. The extra-stress of the PTT model is given as function of the conformation tensor A_{ij} as

$$\tau_{ij} = \frac{\eta_p}{\lambda} (A_{ij} - \delta_{ij}) \quad (4)$$

where η_p is the polymer viscosity parameter, λ is the relaxation time and δ_{ij} is the unitary tensor. The conformation tensor is then described by an evolution equation, which for the PTT fluid takes the form

$$\lambda \left(\frac{\partial A_{ij}}{\partial t} + \frac{\partial u_k}{\partial x_k} A_{ij} - \frac{\partial (u_i A_{kj})}{\partial x_k} - A_{ik} \frac{\partial u_j}{\partial x_k} \right) = -Y[A_{kk}] (A_{ij} - \delta_{ij}) \quad (5)$$

In its general form function $Y[A_{kk}]$ for the PTT model is exponential, $Y[A_{kk}] = \exp[\varepsilon(A_{kk} - 3)]$ (Phan-Thien, 1978), but in this work we will mostly use its linear form, $Y[A_{kk}] = 1 + \varepsilon(A_{kk} - 3)$ (Phan-Thien and Tanner, 1977). When $Y[A_{kk}] = 1$ (i.e. for $\varepsilon = 0$) the Oldroyd-B model is recovered. Additionally, if in the momentum equation we set $\eta_s = 0$ then the UCM model is obtained. The non-unitary form of $Y[A_{kk}]$ for the PTT model imparts shear-thinning behaviour to the shear viscosity of the fluid and bounds its steady-state extensional viscosity.

The tensor A_{ij} is a variance-covariance, symmetric positive definite tensor, therefore it can always be diagonalized as $A_{ij} = O_{ik} L_{ki} (O^T)_{lj}$, where O_{ij} is an orthogonal matrix generated with the eigenvectors of matrix A_{ij} and L_{ij} is a diagonal matrix created with the corresponding three distinct eigenvalues of A_{ij} . This fact provides the possibility of using the log-conformation technique, introduced by Fattal and Kupferman (2004), which has been shown to lead to a significant increase of numerical stability. In this technique a simple tensor-logarithmic transformation is performed on the conformation tensor for differential viscoelastic constitutive equations. This technique can be applied to a wide variety of constitutive laws and in the log-conformation representation the evolution Eq. (5) is replaced by an equivalent evolution equation for the log-conformation tensor, $\Theta = \log(\mathbf{A})$. The transformation from Eq. (5) to an equation for Θ_{ij} is described by Fattal and Kupferman (2004), and leads to

$$\frac{\partial \Theta_{ij}}{\partial t} + u_k \frac{\partial \Theta_{ij}}{\partial x_k} - (R_{ik} \Theta_{kj} - \Theta_{ik} R_{kj}) - 2E_{ij} = -\frac{Y[(e^{\Theta_{ij}})_{kk}]}{\lambda} (e^{-\Theta_{ij}} - \delta_{ij}) \quad (6)$$

In Eq. (6) R_{ij} and E_{ij} are a pure rotational tensor and a traceless extensional tensor, respectively, which combine to form the velocity gradient tensor. To recover A_{ij} from Θ_{ij} the

inverse transformation, $\mathbf{A} = \mathbf{e}^\Theta$, is used when necessary. The log-conformation approach is a relevant particular case of the recently proposed general kernel-conformation tensor transformation (Afonso et al 2012), in which several matrix transformations can be applied to the conformation tensor evolution equation.

After application of the transformation rules introduced above, the conservation equations of mass and momentum become (Oliveira, 1992):

$$\frac{\partial(\rho\beta_{li}u_i)}{\partial\xi_l} = 0 \tag{7}$$

$$\begin{aligned} \frac{\partial(J\rho u_i)}{\partial t} + \frac{\partial(\rho\beta_{lj}u_j u_i)}{\partial\xi_l} - \frac{\partial}{\partial\xi_l} \left(\eta \frac{\beta_{lj}\beta_{lj}}{J} \frac{\partial u_i}{\partial\xi_l} \right) = \\ -\beta_{li} \frac{\partial p}{\partial\xi_l} + \frac{\partial}{\partial\xi_l} (\beta_{lj}\tau_{ij}) + J\rho g_i + \frac{\partial}{\partial\xi_l} \left(\frac{\eta_s \beta_{lj}}{J} \left(\beta_{mj} \frac{\partial u_i}{\partial\xi_m} + \beta_{mi} \frac{\partial u_j}{\partial\xi_m} \right) \right) - \frac{\partial}{\partial\xi_l} \left(\eta \frac{\beta_{lj}\beta_{lj}}{J} \frac{\partial u_i}{\partial\xi_l} \right) \end{aligned} \tag{8}$$

with $l' = l$, and no summation over index l' . Note that although the diffusive term of the momentum equation (the term proportional to η_s) involves only normal second derivatives, its transformation to the non-orthogonal system originates mixed second-order derivatives. The artificial diffusion term added in both sides of Eq. (8) has a viscosity coefficient $\eta = \eta_s + \eta_p$ and is especially necessary when $\eta_s = 0$.

The rheological constitutive equation becomes

$$\lambda \frac{\partial(J\Theta_{ij})}{\partial t} + \lambda \frac{\partial}{\partial\xi_l} (\beta_{lk}u_k\Theta_{ij}) = \lambda J(R_{ik}\Theta_{kj} - \Theta_{ik}R_{kj}) + 2\lambda J E_{ij} + Y(A_{kk})J \left(e^{-\Theta_{ij}} - \delta_{ij} \right) \tag{9}$$

together with Eq. (4) and the inverse transformation $\mathbf{A} = \mathbf{e}^\Theta$.

3.4 Discretization of the equations

The objective of the discretization is to obtain a set of algebraic equations relating centre-of-cell values of the unknown variables to their values at nearby cells. These equations are linearized and the large sets of linear equations are solved sequentially for each variable using well-established iterative methods.

The integration of the governing equations in generalized coordinates is straightforward after an acquaintance with the nomenclature, which is summarized in Figure 2. In the discretization, the usual approximations regarding average unknowns at cell-faces and control volumes apply (for details, see Ferziger and Perić, 2002). For the discretization of the equations in the generalized coordinate system, it suffices to replace the coefficients β_{li} by area components of the surface along direction l , denoted B_{li} , the Jacobian J by the cell volume V , and the derivatives $\partial/\partial\xi_l$ by differences between values along direction l ,

$$\frac{\partial\Phi}{\partial\xi_l} = [\Delta\Phi]_l \equiv \Phi_{l^+} - \Phi_{l^-} \tag{10}$$

These differences and the area components can be evaluated at two different locations:

1. at cell centres, here denoted with the superscript P,

$$[\Delta\Phi]_f^P \equiv \Phi_{f^+} - \Phi_{f^-} \quad \text{and} \quad B_{fi}^P \tag{11}$$

2. at cell-faces, with superscript f,

$$[\Delta\Phi]_f^f \equiv \Phi_F - \Phi_P \quad \text{and} \quad B_{fi}^f \tag{12}$$

In this notation, index F denotes the centre of the neighbour cell to the generic cell P sharing the same face f (see Figure 2), therefore these two indices, f and F are associated; double characters (FF and ff) refer to the second neighbour and cell face, respectively, along the same direction.

In the discretized equations, variables at a general cell P and at its six neighbours (F = 1 to 6, for W, E, S, N, B and T with compass notation: west, east, south, north, bottom and top, i.e. for $l = \mp 1, \mp 2$ and ∓ 3 , respectively) are treated implicitly and form the main stencil in the discretization. The six far-away neighbours (FF=1 to 6, for WW, EE, SS, NN, BB and TT) appearing in high order schemes, give rise to contributions which are incorporated into the so-called source term and are treated explicitly being evaluated from known values from the previous iteration/time-step. Thus, the linearized sets of equations for each dependent variable, which need to be solved at every time step, have a well defined block-structured matrix with 7 non-zero diagonals. This is one important difference with the finite-element method, which gives rise to banded matrices with no particular structure inside the band.

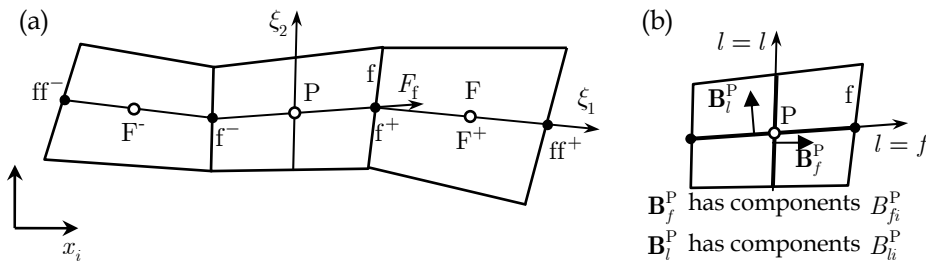


Fig. 2. Nomenclature: (a) general and neighbouring cells; (b) area vectors and components.

3.4.1 Continuity equation

The continuity equation is volume integrated and discretized as follows (sums are explicitly indicated in the discretized equations):

$$\int_{V_P} \frac{\partial}{\partial \xi_l} (\rho \beta_{ij} u_j) dV = 0 \rightarrow \sum_{l=1}^3 \left[\Delta \left(\sum_j \rho B_{ij} u_j \right) \right]_l^P = \sum_{f=1}^6 \left(\sum_j \rho B_{fj}^f \tilde{u}_{j,f} \right) = \sum_{f=1}^6 F_f = 0 \tag{13}$$

In this equation, the sum of differences centred at cell centre P has been transformed into a sum of contributions arising from the six cell faces, f. The tilde in $\tilde{u}_{j,f}$, referring to the cell face

velocity component u_j , means that this cannot be computed from simple linear interpolation, in which case no special symbol would be required according to our nomenclature, but need to be evaluated via a kind of Rhie and Chow (1983) interpolation technique, to be explained in Section 3.6. It is this special interpolation that ensures coupling between the pressure and velocity fields in a collocated mesh arrangement. Considering the definition of outgoing mass flow rates (F_f), the discretized continuity equation expresses the fact that the sum of incoming mass flow rates (negative) equals the sum of out-going flow rates (positive).

3.4.2 Momentum equation

The integration of each term in Eq. (8), starting from left to right, results in the following algebraic expressions.

Inertial term: This term does not benefit from the application of Gauss’ theorem; hence its discretization results in

$$\int_{V_p} \frac{\partial}{\partial t} (J\rho u_i) dV = \frac{\rho V_p}{\delta t} (u_{i,P} - u_{i,P}^{(n)}) \tag{14}$$

where $u_{i,P}^{(n)}$ is the velocity at cell P at the previous time level and V_p represents the volume of cell P. The present method is fully implicit meaning that all variables without a time-level superscript are assumed to pertain to the new time-level ($n + 1$). The superscript (n) denotes a previous time step value. More accurate discretization procedures can be introduced for time-dependent calculations, but at this stage we use the implicit first-order Euler method for simplicity.

Convection term: As in Eq. (13), this term benefits from Gauss’ theorem,

$$\int_{V_p} \frac{\partial}{\partial \xi_l} (\rho \beta_{ij} u_j u_i) dV = \sum_{l=1}^3 \left[\Delta \left(\sum_j (\rho \beta_{ij} u_j) u_i \right) \right]_l^P = \sum_{f=1}^6 F_f \hat{u}_{i,f} \tag{15}$$

with the cell face mass fluxes defined as in Eq. (13) and the convected velocity at face f , $\hat{u}_{i,f}$, being given according to the discretization scheme adopted for the convective terms. For the upwind differencing scheme, $\hat{u}_{i,f}$ is simply the velocity at the centre of the cell in the upwind direction, which can be written generally by expressing the convection fluxes of momentum as

$$F_f \hat{u}_{i,f} = F_f^+ u_{i,P} + F_f^- u_{i,F} \quad \text{where } F_f^+ \equiv \text{Max}(F_f, 0) \text{ and } F_f^- \equiv \text{Min}(F_f, 0) \tag{16}$$

Diffusion term: A normal diffusion term is added to both sides of the momentum equation, Eq. (8), in order to obtain a standard convection-diffusion equation when there is no solvent viscosity contribution, $\eta_s = 0$. This choice is akin to the Elastic Viscous Stress Splitting approach (Perera and Walters, 1977; Rajagopalan et al, 1990). The term added to the left hand side of the equation is given by the following expression, and discretized as shown:

$$-\int_{V_p} \frac{\partial}{\partial \xi_l} \left(\frac{\eta}{J} \beta_{l,j} \beta_{l,j} \frac{\partial u_i}{\partial \xi_l} \right) dV = -\sum_{f=1}^6 \frac{\eta_f B_f^2}{V_f} [\Delta u_i]_f = -\sum_{f=1}^6 D_f (u_{i,F} - u_{i,P}) \tag{17}$$

where the surface area of the cell face is $B_f = \sqrt{\sum_j B_{ff}^f B_{ff}^f}$, the volume of a pseudo-cell centred

at the face is $V_f = \sum_{j=1}^3 B_{ff}^f [\Delta x_j]_f^f$, and $D_f \equiv \eta_t B_f^2 / V_f$ is a diffusion conductance. An identical

term is added to the right hand side of the momentum equation, where it is treated explicitly and added to the source term. When iterative convergence is achieved, these two terms cancel out exactly. The solvent viscosity contribution is discretised using a similar approach.

Pressure gradient term: The pressure gradient is centred at P, thus leading to pressure differences across cell-widths. In representing it as S_{u_i} , it is implied that it will become a contribution to the source term of the algebraic equation, and therefore will be calculated explicitly as:

$$-\int_{V_p} \beta_{ii} \frac{\partial p}{\partial \xi_l} dV = -\sum_{l=1}^3 B_{ii}^p [\Delta p]_l^p \equiv S_{u_i - pressure} \quad (18)$$

Stress-divergence term: Another term benefiting from Gauss' theorem, it becomes

$$\int_{V_p} \frac{\partial}{\partial \xi_l} (\beta_{ij} \tau_{ij}) dV = \sum_{f=1}^6 B_{ff}^f \tilde{\tau}_{ij,f} \equiv S_{u_i - stress} \quad (19)$$

where, like with the face velocity in the continuity equation beforehand, the cell-face stress (denoted with tilde) requires a special interpolation method due to the use of the collocated mesh arrangement. The way to do this constitutes one of the contributions of our work and is essential for the applicability of this method described in Section 3.7. This term is also treated explicitly in the context of the momentum equation, i.e. it becomes part of the momentum source term.

Gravity or body-force term: As with the pressure gradient term, this contribution is calculated at the cell centre and is included in the source term of momentum equation,

$$\int_{V_p} J \rho g_i dV = \rho V_p g_i \equiv S_{u_i - gravity} \quad (20)$$

The final discretized form of the momentum equation is obtained at after re-grouping the various terms discussed above, to give:

$$a_p u_{i,P} - \sum_F a_F u_{i,F} = S_{u_i} + \frac{\rho V_p}{\delta t} u_{i,P}^{(n)} \quad (21)$$

where the coefficients a_F consist of convection (a_F^C , here based on the upwind differencing scheme (UDS)) and diffusion contributions (a_F^D):

$$a_F = a_F^D + a_F^C, \text{ with } a_F^D = D_f \text{ and}$$

$$a_F^C = \begin{cases} -F_f^- & \text{(for a negative face, } f^-) \\ +F_f^+ & \text{(for a positive face, } f^+) \end{cases} \quad (22)$$

The central coefficient is:

$$a_P = \frac{\rho V_P}{\delta t} + \sum_F a_F \quad (23)$$

and the total source term is given by the sum

$$S_{u_i} = S_{u_i\text{-pressure}} + S_{u_i\text{-gravity}} + S_{u_i\text{-stress}} + S_{u_i\text{-diffusion}} \quad (24)$$

The source term S_{u_i} may contain additional contributions, such as those resulting from the application of boundary conditions, the use of high-resolution schemes for convection, or previous time step values for higher-order time-discretization schemes, amongst others.

3.4.3 Rheological constitutive equation

The two terms on the left hand side of Eq. (9) are discretized as the inertia (Eq. 14) and the convection terms above (Eq. 15), respectively, and do not present any additional difficulty. It should be noted that in all terms the velocity component u_i is replaced by τ_{ij} , and the mass flow rates in the convective fluxes, defined in Eq. (13), should be multiplied by λ/ρ (compare the convective fluxes in Eqs. 8 and 9). Following the same approach as above, the source term in the stress conformation tensor constitutive equation becomes:

$$S_{\Theta_{ij}} = \lambda V_P \left[R_{ik} \Theta_{kj} - \Theta_{ik} R_{kj} \right]_P + 2\lambda V_P E_{ij,P} + Y(A_{kk,P}) V_P \left(e^{-\Theta_{ij,P}} - \delta_{ij} \right) \quad (25)$$

The final form of the linearized equation is therefore

$$a_P^\Theta \Theta_{ij,P} - \sum_F a_F^\Theta \Theta_{ij,F} = S_{\Theta_{ij}} + \frac{\lambda V_P}{\delta t} \Theta_{ij,P}^{(n)} \quad (26)$$

with the coefficients a_F^Θ consisting of the convective coefficients in Eq. (22) multiplied by λ/ρ , for the reasons just explained, and the central coefficient is:

$$a_P^\Theta = V_P + \sum_F a_F^\Theta + \frac{\lambda V_P}{\delta t} = V_P + a_0^\Theta|_P + \frac{\lambda V_P}{\delta t} \quad (27)$$

Whenever the extra-stress tensor is used in the code, it can be recovered from the conformation tensor using Eq. (4).

3.5 High-resolution schemes

The convective terms of the momentum and constitutive equations contain first derivatives of transported quantities, therefore an interpolation formula for their determination at cell

faces is required ($\hat{u}_{i,f}$ in Eq. 15 and $\hat{\Theta}_{ij,f}$ in the convection term of the constitutive equation). In the previous section the UDS was used for such purpose, in particular for the determination of the convected velocities at cell-faces in Eq. (16). The upwind scheme is the most stable of all the schemes for convection, but has only first order accuracy and therefore gives rise to excessive numerical diffusion. Such problem is aggravated for the hyperbolic-type conformation equations.

Higher order methods for improved calculations have been widely used in CFD, such as second- and third-order upwind schemes (e.g. the QUICK scheme developed by Leonard, 1991). However, these schemes suffer from stability or iterative convergence problems, and are often not limited. To address these difficulties various differencing schemes have been combined in what are called high-resolution schemes (HRS). These methods ensure better convergence and stability properties and are generally bounded to avoid the appearance of spurious oscillations in regions with high gradients of the transported quantity.

The calculation of viscoelastic fluid flows has its own specificities, which are well described in specialized works (e.g. Owens and Phillips, 2002). For instance, HRS with good performance for Newtonian fluids often have problems of convergence and stability with viscoelastic fluids, as discussed by Alves et al (2003a), who developed an HRS particularly adequate for computational rheology, the CUBISTA scheme (Convergent and Universally Bounded Interpolation Scheme for the Treatment of Advection). This HRS is described below as implemented in our viscoelastic flow solver.

In what regards implementation of the HRS we use the so-called deferred correction approach of Khosla and Rubin (1974), where the convective contributions to the coefficients a_F and a_P are based on the upwind scheme UDS, to ensure positive coefficients for enhanced stability. The difference between the convective fluxes calculated by the HRS and UDS are handled explicitly and are included in the source term. Therefore, the deferred correction provides stability, simplicity of implementation (avoids increasing the computational stencil) and savings in computer memory, since the coefficients a_P and a_F are the same in the three momentum equations, and a_P^\ominus and a_F^\ominus are also the same in the six stress equations for 3D problems. For time-dependent flows, the use of the deferred correction leads to problems similar to those created by the added diffusive terms of the momentum equation, and the solution is the same: it is necessary to ensure that the added terms cancel each other at each time step by using an iterative procedure within the time-step.

Taking into account the use of the HRS in the scope of the deferred correction, the discretized momentum and constitutive equations can be rewritten as

$$a_P u_{i,P} - \sum_F a_F u_{i,F} = S_{u_i} + \frac{\rho V_P}{\delta t} u_{i,P}^{(n)} + \left(\sum_f F_f \hat{u}_{i,f} \right)_{\text{UDS}}^* - \left(\sum_f F_f \hat{u}_{i,f} \right)_{\text{HRS}}^* \quad (28)$$

$$a_P^\ominus \Theta_{ij,P} - \sum_F a_F^\ominus \Theta_{ij,F} = S_{\Theta_{ij}} + \frac{\lambda V_P}{\delta t} \Theta_{ij,P}^{(n)} + \left(\sum_f \frac{\lambda}{\rho} F_f \hat{\Theta}_{ij,f} \right)_{\text{UDS}}^* - \left(\sum_f \frac{\lambda}{\rho} F_f \hat{\Theta}_{ij,f} \right)_{\text{HRS}}^* \quad (29)$$

In both equations the new terms are evaluated at the previous iteration level (indicated by *) and are included in the source term (S_{u-HRS} and $S_{\Theta-HRS}$).

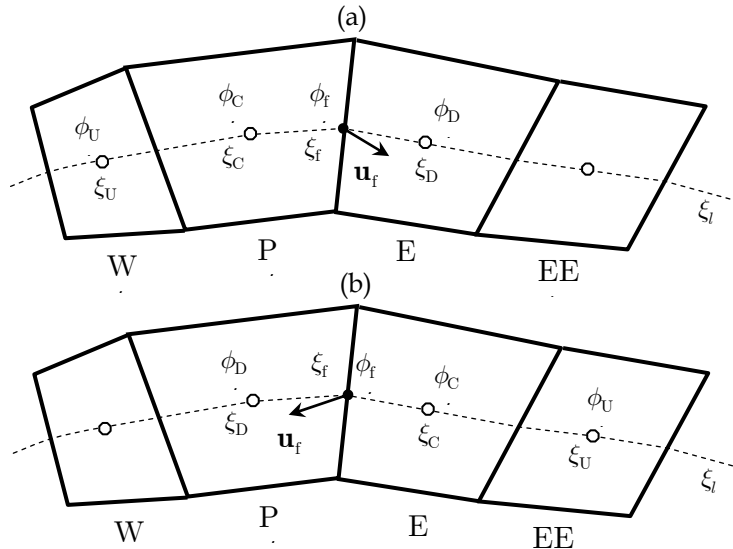


Fig. 3. Definition of local variables and coordinates in the vicinity of face f . (a) Positive velocity along direction ξ_i ; (b) negative velocity along direction ξ_i .

The high-resolution schemes are usually written in compact form, using the normalized variable and space formulation of Darwish and Moukalled (1994). In this formulation the transported quantity ϕ (u_i or Θ_{ij}) and the system of general coordinates ξ , shown schematically in Figure 3, are normalized as

$$\hat{\phi} = \frac{\phi - \phi_U}{\phi_D - \phi_U} \tag{30}$$

$$\hat{\xi} = \frac{\xi - \xi_U}{\xi_D - \xi_U} \tag{31}$$

where subscripts U and D refer to upwind and downwind cells relative to C, which is immediately upstream of face f . The objective is the calculation of ϕ at cell-face f , via a special interpolation scheme for convection ($\hat{\phi}_f$).

In order to satisfy the convection boundedness criterion (CBC) of Gaskell and Lau (1988) the functional relationship of an interpolation scheme applied to a cell face f , $\hat{\phi}_f = fn(\hat{\phi}_C)$, must be continuous and bounded from below by $\hat{\phi}_f = \hat{\phi}_C$ and from above by unity, in the monotonic range $0 < \hat{\phi}_C < 1$. However, the CBC is not sufficient to guarantee that a limited scheme has good iterative convergence properties and therefore Alves et al (2003a) also used the ‘‘Universal Limiter’’ of Leonard (1991), which is valid for explicit transient calculations and reduces to Gaskell and Lau’s criterion for steady flows, when the Courant number tends to zero. On the other hand, the conditions for an explicit time-dependent method to be Total Variation Diminishing are even more restrictive than the universal limiter and it was

based upon these more restrictive conditions that the CUBISTA scheme was formulated to guarantee stability and good iterative convergence properties. The CUBISTA HRS is based on the third-order discretization QUICK scheme, it avoids sudden changes in slope of the functions and ensures limitation of ϕ on the downwind side to preclude ϕ being higher than ϕ_D in its proximity. All these details are extensively discussed in Alves et al (2003a), and give rise to the following function for CUBISTA in non-uniform meshes,

$$\hat{\phi}_f = \begin{cases} \left[1 + \frac{\hat{\xi}_f - \hat{\xi}_C}{3(1 - \hat{\xi}_C)} \right] \frac{\hat{\xi}_f}{\hat{\xi}_C} \hat{\phi}_C & 0 < \hat{\phi}_C < \frac{3}{4} \hat{\xi}_C \\ \frac{\hat{\xi}_f(1 - \hat{\xi}_f)}{\hat{\xi}_C(1 - \hat{\xi}_C)} \hat{\phi}_C + \frac{\hat{\xi}_f(\hat{\xi}_f - \hat{\xi}_C)}{1 - \hat{\xi}_C} & \frac{3}{4} \hat{\xi}_C \leq \hat{\phi}_C \leq \frac{1 + 2(\hat{\xi}_f - \hat{\xi}_C)}{2\hat{\xi}_f - \hat{\xi}_C} \hat{\xi}_C \\ 1 - \frac{1 - \hat{\xi}_f}{2(1 - \hat{\xi}_C)} (1 - \hat{\phi}_C) & \frac{1 + 2(\hat{\xi}_f - \hat{\xi}_C)}{2\hat{\xi}_f - \hat{\xi}_C} \hat{\xi}_C < \hat{\phi}_C < 1 \\ \hat{\phi}_C & \hat{\phi}_C < 0 \text{ and } \hat{\phi}_C > 1 \end{cases} \quad (32)$$

where $\hat{\phi}_C$, $\hat{\xi}_C$ and $\hat{\xi}_f$ are defined in Eqs. (30) and (31).

3.6 Formulation of the mass fluxes at cell faces

The mass flow rates (F_f) in coefficients a_f^C and a_f^P have to be calculated with velocities at cell faces ($\tilde{u}_{i,f}$), which must be related to velocities at cell centres. The need to calculate $\tilde{u}_{i,f}$ at a cell face is a consequence of the use of collocated meshes and would not occur if staggered meshes were used. The continuity equation is needed to solve for the pressure field, after a velocity field is calculated from the momentum equation as in the SIMPLE procedure initially developed by Patankar and Spalding (1972) using staggered meshes for the calculation of the velocity and pressure fields. Here, each velocity component data are stored in meshes staggered by half a cell width relative to the original mesh where the scalar quantities are stored and in this way the coupling between velocity and pressure is naturally ensured while momentum and mass is conserved.

By using a single non-orthogonal mesh with the collocated variable arrangement, coupling between the velocity and pressure fields needs a special interpolation scheme to calculate velocities at cell-faces otherwise even-odd oscillations in the pressure or velocity fields may occur. The key idea to solve this decoupling problem was proposed by Rhie and Chow (1983). Oliveira (1992) and Issa and Oliveira (1994) adapted that idea for their time-marching algorithm under a slightly modified form explained hereafter.

The momentum equation (Eq. 21) at node P can be rewritten as

$$a_p u_{i,P} = \sum_F a_F u_{i,F} - \sum_{l=1}^3 B_{li}^P [\Delta p]_l^P + S_{u_i}^P + \left(\frac{\rho V}{\delta t} \right)_P u_{i,P}^{(n)} \quad (33)$$

where the pressure term was extracted from the source term and is written explicitly with a pressure difference evaluated at a cell centre (i.e. $[\Delta p]_l^P = p^{l+} - p^{l-}$, cf. Figure 2).

According to Rhie and Chow’s special interpolation method, the cell face velocity \tilde{u}_f is calculated by linear interpolation of the momentum equation, with exception of the pressure gradient which is evaluated as in the original method of Patankar and Spalding for staggered meshes. This idea is applied as described in Issa and Oliveira (1994), by writing

$$\bar{a}_p \tilde{u}_{i,f} = \sum_F \overline{a_{F,i,F}} + \overline{S'_{u_i}} - B_{\tilde{f}}^f [\Delta p]_f^f - \sum_{l \neq f} \overline{B_{li} [\Delta p]_l} + \left(\frac{\rho V}{\delta t} \right)_P \tilde{u}_{i,f}^{(n)} \tag{34}$$

where the overbar denotes here an arithmetic mean of quantities pertaining to cells P and F. Notice that the pressure difference along direction $l = f$ is now evaluated at cell-face (i.e. $[\Delta p]_f^f = p_F - p_P$), whereas the pressure at cell faces pertaining to directions $l \neq f$ are calculated by linear interpolation of the nodal values of pressure. With this approach the velocity at face f is directly linked to pressures calculated at neighbour cell centres, as in the staggered arrangement, and pressure-velocity decoupling is prevented.

By subtracting Eq. (34) from the averaged momentum equation resulting from averaging all terms of Eq. (33) the following face-velocity equation used to compute F_f is obtained:

$$\tilde{u}_{i,f} = \frac{\overline{a_p u_{i,P}} + \overline{B_{\tilde{f}}^p [\Delta p]_f^p} - B_{\tilde{f}}^f [\Delta p]_f^f + \left(\frac{\rho V}{\delta t} \right)_P \tilde{u}_{i,f}^{(n)} - \left(\frac{\rho V}{\delta t} u_{i,P}^{(n)} \right)_P}{\bar{a}_p} \tag{35}$$

3.7 Formulation of the cell-face stresses

In the momentum equation it is necessary to compute the stresses at cell faces ($\tilde{\tau}_{ij,f}$ in Eq. 19) from stress values at neighbouring cell centres and there is a stress-velocity coupling problem, akin to the pressure-velocity coupling of the previous subsection. If a linear interpolation of cell centred values of stress is used to compute those face values, a possible lack of connectivity between the stress and velocity fields may result, even with Newtonian fluids, as shown by Oliveira et al (1998). The methodology described here is based on the works of Oliveira et al (1998), Oliveira and Pinho (1999a) and more recently by Matos et al (2009) and constitutes a key ingredient for the success of viscoelastic flow computations with the finite-volume method on general, non-orthogonal, collocated meshes. Following the ideas of Matos et al (2009), the extra-stress at face f is computed as

$$\tilde{\tau}_{ij,f} = \left(\overline{\tau_{ij}} \right)_f + \frac{\eta}{\left(1 + \alpha_0^0 / V \right)} \left[\frac{1}{V_f} \left(B_{\tilde{f}} [\Delta u_j]_f + B_{\tilde{f}} [\Delta u_i]_f \right) - \frac{1}{V} \left(B_{\tilde{f}} [\Delta u_j]_f + B_{\tilde{f}} [\Delta u_i]_f \right) \right] \tag{36}$$

where the $\overline{\tau_{ij}}$ denotes a linear interpolation rather than an arithmetic mean. It is obvious from Eq. (36) that the extra-stress at face f ($\tilde{\tau}_{ik,f}$) is now directly coupled to the nearby cell-centre velocities, through the term in $[\Delta u_i]_f^f = u_{i,F} - u_{i,P}$, inhibiting the undesirable decoupling between the stress and velocity fields. In Matos et al (2009) the standard formulation for the constitutive equation was used, based on the extra-stress tensor, and Eq. (36) results directly from the discretization of the extra-stress tensor equation. Here we use the log-conformation methodology, but since the central coefficients of the discretized equations for the extra-stress and for the log-conformation tensors are the same, then Eq. (36) is still applicable.

3.8 Solution algorithm

As in any pressure correction procedure (e.g. Patankar and Spalding, 1972), pressure is calculated indirectly from the restriction imposed by continuity, since the momentum equation, which explicitly contains a pressure gradient term, is used to compute the velocity vector components. The SIMPLEC algorithm of Van Doormal and Raithby (1984) is followed here under a modified form. The original SIMPLEC algorithm was developed for iterative steady flow calculations, but the time-marching version described in Issa and Oliveira (1994) offers some advantages and is used here instead. Time marching allows for the solution of transient flows provided the time step is sufficiently small, with the added advantage that it can be used for steady flows as an alternative to implement under-relaxation.

The incorporation of a rheological constitutive equation produces little changes on the original SIMPLEC method developed for Newtonian fluids, which is mainly concerned with the calculation of pressure from the continuity equation. An overview of the solution algorithm is now given, including the new steps related to the stress calculation:

1. Initially, the conformation tensor A_{ij} , calculated from the extra-stress components τ_{ij} via Eq. (4). At each point the eigenvalues and eigenvectors of A_{ij} are computed and the conformation tensor is diagonalized to calculate Θ_{ij} .
2. The tensors R_{ij} and E_{ij} are calculated, following the procedure described in Fattal and Kupeferman (2004).
3. The discretized form of the evolution equation for Θ_{ij} in Eq. (37) is solved to obtain Θ_{ij} at the new time level,

$$a_P^\Theta \Theta_{ij,P}^* - \sum_F a_F^\Theta \Theta_{ij,F}^* = S_{\Theta_{ij}} \quad (37)$$

where the coefficients and source term of these linear equations are based on the previous iteration level variables, and Θ_{ij}^* denotes the new time-level of Θ_{ij} .

4. The conformation tensor A_{ij} is recovered and the extra-stress tensor is calculated from the newly computed conformation field using Eq. (4).
5. The momentum equation (38) is solved implicitly for each velocity component, u_i :

$$\left(\sum_F a_F + \frac{\rho V_P}{\delta t} \right) u_{i,P}^* - \sum_F a_F u_{i,F}^* = \sum_l B_{li} [\Delta p^*]_l^P + S_{u_i} + \frac{\rho V_P}{\delta t} u_{i,P}^{(n)} \quad (38)$$

where the pressure gradient term is based on previous iteration level pressure field and has been singled out of the remaining source term for later convenience. The stress-related source term (Eq. 19) is based on newly obtained cell-face stress $\tilde{\tau}_{ij}^{*f}$, calculated from Eq. (36), which requires the central coefficient of the log-conformation tensor equation (a_P^Θ). This is the main reason for solving the constitutive equation before the momentum equation.

6. Starred velocity components (u_i^*) do not generally satisfy the continuity equation. The next step of the algorithm involves a correction to u_i^* , so that an updated velocity field u_i^{**} will satisfy both the continuity equation and the following split form of the momentum equation:

$$\sum_F a_F u_{i,P}^{**} + \frac{\rho V_P}{\delta t} u_{i,P}^{**} = \sum_F a_F u_{i,F}^* - \sum_l B_{li} [\Delta p^{**}]_l^P + S_{u_i} + \frac{\rho V_P}{\delta t} u_{i,P}^{(n)} \quad (39)$$

It is noted that in Eq. (39) only the time-dependent term is updated to the new iteration level u_i^{**} , a feature of the SIMPLEC algorithm (Issa and Oliveira, 1994). Subtraction of this equation from Eq. (38) and forcing the u_i^{**} field to satisfy continuity ($\sum_f F_f^{**} = 0$, cf.

Eq. 13) leads to the pressure correction and velocity correction equations (Eqs. 40 and 41, respectively, where $p' = p^{**} - p^*$):

$$a_P^p p'_P = \sum_F a_F^p p'_F - \sum_f F_f^* \quad a_P^p = \sum_F a_F^p; a_F^p = \left(\frac{\rho B_f^2}{\frac{\rho V}{\delta t}} \right)_f \tag{40}$$

$$\frac{\rho V_P}{\delta t} (u_i^{**} - u_i^*)_P = - \sum_l B_{il}^p [\Delta p']_l^P \tag{41}$$

7. Steps 1-6 are repeated until overall convergence is reached (steady-state calculations), or convergence within a time step (unsteady calculations) followed by advancement until the desired final time is reached.

The various sets of algebraic equations are solved with either a symmetric or a bi-conjugate gradient method for the pressure and the remaining variables, respectively (Meijerink and Van der Vorst, 1977). In both cases the matrices are pre-conditioned by an incomplete LU decomposition.

3.9 Boundary conditions

Appropriate boundary conditions are required for the dependent variables (u_i, p and Θ_{ij}) at the external boundary faces of the flow domain. Four types of boundaries are typically encountered in the applications considered in this work, namely inlets, outlets, symmetry planes and walls. Each one is dealt with briefly below and the interested reader is referred to specific literature for more details.

Inlet: Velocity and stress components are given according to some pre-specified profiles (from theory or measured data), and Θ_{ij} is calculated accordingly. Sometimes the streamwise velocity at inlet is set equal to a uniform value and a null stress field is considered, but most often fully developed flow conditions are assumed for velocity and stress fields. Progress on work dealing with derivation of analytical solutions for viscoelastic models has been made during the past years, and velocity and stress distributions in fully developed duct flows can be found in Oliveira and Pinho (1999c) for the PTT model, Alves et al (2001b) for the full PTT model and Oliveira (2002) for the FENE-P model, amongst other solutions. These are useful not only to prescribe inlet conditions but also to obtain the wall boundary conditions where the convective terms in the equations are null, as for fully developed flow.

Outlet: The outlet planes are located far away from the main region of interest, where the flow can be assumed fully developed. Thus, zero streamwise gradients are prescribed for the velocity, the Θ_{ij} components and the pressure gradient. The latter is equivalent to a linear extrapolation of pressure values from the two internal cells to the outlet boundary face. An

additional condition required by the pressure correction equation in incompressible flow is to adjust the velocities at the boundary faces so that overall mass conservation is satisfied.

Symmetry planes: Across a symmetry plane the convective and diffusive fluxes must vanish. These two conditions are applied to all variables using reflection rules in fictitious symmetric cells (Figure 4a) and result in the following procedure to implement these boundary conditions (see Oliveira and Pinho, 1996b for details). At the symmetry plane there is only tangential velocity, i.e. the normal velocity is null. So, at the face coincident with the symmetry plane $u_{i,f}^n = 0$ and $u_{i,f}^t = u_{i,f}$ (superscripts n and t denote normal and tangential components, respectively). Since the fictitious cell P' is symmetric to cell P, the calculation of the components of the velocity vector u_i at the cell face f ($u_{i,f}$) is obtained by linear interpolation from the velocities at the adjacent cell nodes leading to

$$u_{i,f} = u_{i,f}^t = u_{i,p} - u_p^n \cdot n_i \text{ and } u_p^n = \sum_j u_{j,p} n_j \tag{42}$$

where u_p^n is the component of the velocity vector normal to the symmetry plane and n_i is the i -component of the unit vector normal to the symmetry plane.

For scalar quantities, such as the pressure, the reflexion rule at symmetry planes leads to

$$p_f = p_p \tag{43}$$

Imposition of boundary conditions for the stress is facilitated by recognizing that not all individual stress components are required at the cell face f coincident with the symmetry plane, since the tangential stress vector is zero. Therefore, as seen from Eq. (19), the contribution from face f to the total stress source at cell P is just:

$$\left(S_{u_i-stress} \right)_f = \sum_j B_{ff}^f \tau_{ij,f} = B_f \sum_j \tau_{ij,f} n_j \text{ leading to } \left(S_{u_i-stress} \right)_f = T_{n,p} B_{fi} = T_{n,p} B_f n_i \tag{44}$$

where the unit normal vector is computed as $n_j = B_{ff} / B_f$. Thus, the boundary condition at the symmetry plane represents only the traction vector normal to face f .

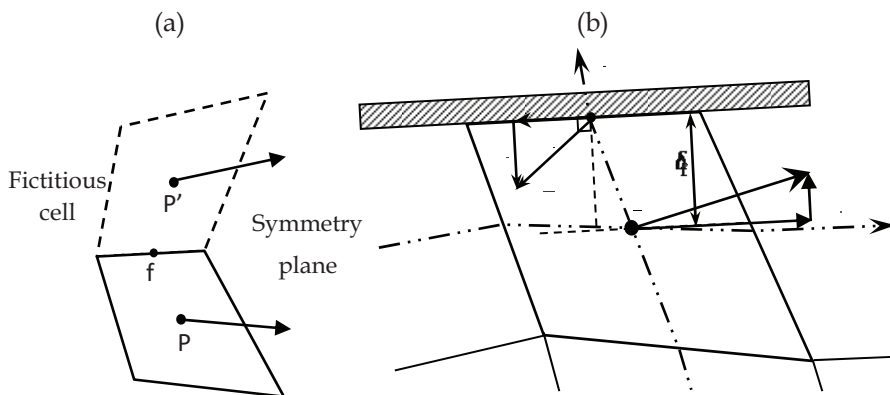


Fig. 4. Cells at boundaries: (a) The fictitious cell adjacent to a symmetry plane; (b) Schematic representation of an internal cell adjoining a wall.

Walls: At walls additional problems in imposing boundary conditions arise, especially for pressure and the stresses. Those problems are more severe when the constitutive equation predicts non null stresses normal to walls, as in the Giesekus or full PTT models. Boundary conditions for the velocity field are easy to impose. For a wall moving at velocity u_w , the no slip condition for the components u_i of the velocity vector are simply

$$u_{i,f} = u_{i,w} \tag{45}$$

More generally, for a non-porous wall this is mathematically expressed as $u_{i,f}^n = 0$ and $u_{i,f}^t = u_{i,w}$ which are numerically obtained by linear interpolation from velocities at cells adjacent to the wall.

Boundary conditions for stresses are based on the assumption that the flow in the vicinity of a wall is parallel to this boundary, i.e. it is locally a Couette flow. This assumption allows a relatively easy implementation of boundary conditions provided the rheometric material functions of the fluid model are known. A complete explanation of the procedure can be found in Oliveira (2001) and the main points are given here.

Consider Figure 4b which shows the inner cell next to a wall plane. The stress vector near the wall $T_i = \sum_j \tau_{ij} n_j$ has tangential and normal components to the wall ($T_i = T_i^t + T_i^n$). Since

the near wall flow is assumed to be a Couette flow, the tangential component of the traction vector is calculated as

$$T_i^t = \mu(\dot{\gamma}) \frac{\partial u_{i,f}^t}{\partial n} \rightarrow T_i^t = \mu(\dot{\gamma}_f) \frac{u_{i,f}^t - u_{i,P}^t}{\delta_f} \tag{46}$$

where n is the vector normal to the wall and $\mu(\dot{\gamma})$ is the shear viscosity material function of the constitutive model (not to be confused with the parameter η of the constitutive equation), which depends on the invariant $\dot{\gamma}$ of the rate of deformation tensor. This wall shear rate is equal to $\partial u_{i,f}^t / \partial n$ and is calculated as in Eq. (46), where δ_f is the distance from f to the cell centre P along the normal to the wall (see Figure 4b).

Note that in the finite volume method the discretization of the traction vector is indeed carried out as a component of the momentum equation and appears as the result of the integration and subsequent discretization of the term (19), now applied to a wall. Here

$$(S_{u_i-stress})_f = \left(B \sum_j \tau_{ij} n_j \right)_f = B_f T_{i,f} = B_f (T_i^t + T_i^n)_f \tag{47}$$

has two contributions: one associated to the tangential stress, given by Eq. (46), and the other due to normal stress at the face which is null for constitutive models with $N_2 = 0$ as those used for the computations in Section 4. For constitutive models with $N_2 \neq 0$, such as the Giesekus or the full PTT, the interested reader is referred to Oliveira (2001) for the determination of T_i^n .

Finally, we must consider the wall boundary condition for pressure. It is usual practice in CFD to extrapolate linearly the pressure to the wall from the two nearest neighbour cells (Ferziger and Perić, 2002) and this practice also works well for some viscoelastic fluids. However, in viscoelastic flow with fluids exhibiting strong normal stresses perpendicular to the wall ($N_2 \neq 0$), pressure extrapolation is not satisfactory and a better formulation can be derived from the momentum equation normal to the wall at the interior point P, as explained in detail in Oliveira (2001), leading to the following corrected extrapolation formula (a_p is the central coefficient in the momentum equation)

$$p_f = 2p_p - p_{f^-} + \frac{a_p u_{n,P}}{B_f} \quad (48)$$

The two first terms on the right-hand-side of this equation do correspond to linear extrapolation from the two nearest neighbour cells and the last term is a correction which decreases as the mesh is refined close to a wall.

4. Benchmark results in 4:1 planar sudden contraction flows

In this section we assess the capabilities of the finite-volume method described previously by presenting results of simulations for the benchmark flow through a 4:1 planar sudden contraction shown in Figure 5 under conditions of negligible inertia. This is a long standing classic benchmark in computational rheology (Hassager, 1988), where the difficulty lies at the correct prediction of the large stresses and stress gradients in the vicinity of the re-entrant corner (generally all models show the stresses to grow to infinity as the corner is approached) making this flow very sensitive to highly elastic flows. In particular, it is important to know the upstream vortex growth mechanisms due to flow elasticity, and the corresponding large pressure drops and overshoot of the axial velocity along the centreline.

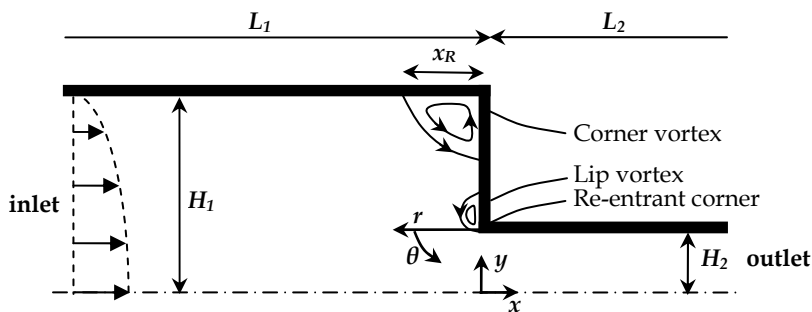


Fig. 5. Schematic representation of a sudden contraction.

4.1 Experimental results

Experiments on sudden contraction flows have been carried out since the 19th century and their characteristics for Newtonian and purely viscous non-Newtonian fluids are well known, especially for the axisymmetric case (cf. the review of Boger, 1987). Contraction flows are very sensitive to fluid properties as well as to geometric characteristics, especially

the contraction ratio (CR). Therefore, we must distinguish the flow in either planar or axisymmetric contractions, and between elastic fluids having constant viscosity (Boger fluids) and shear-thinning viscosity, as well as fluids having different behaviour in extensional flow (Boger, 1987).

In the circular contraction arrangement, whereas for some fluids there is corner vortex enhancement with fluid elasticity, for some Boger fluids a lip vortex appears first and grows with elasticity while the corner vortex decreases. Then, as elasticity further increases, the lip vortex engulfs the corner vortex, becomes convex and it continues to grow with fluid elasticity until the onset of flow instabilities (Boger et al, 1986). For better understanding, these flow features are illustrated in the sketch of Figure 5.

For the 4:1 planar contraction, the early investigations with Boger fluids by Walters and Webster (1982) did not find any peculiar flow feature, in contrast to their behaviour in a circular 4.4:1 contraction. To help clarify this issue, Evans and Walters (1986, 1989) visualized the flow of shear-thinning elastic fluids in 4:1, 16:1 and 80:1 contractions, and reported elastic vortex growth, even in the smaller CR , showing also that an increased CR intensified the phenomenon. They also found a lip vortex for the two larger CR .

To conclude, for shear-thinning fluids there was elastic vortex growth for both the 4:1 planar and circular contractions whereas for Boger fluids the vortex growth was reported only to occur for the axisymmetric geometry. This was confirmed experimentally by Nigen and Walters (2002), who looked at the behaviour of Boger and Newtonian fluids having the same shear viscosity, in 4:1 and 32:1 sudden contractions: whereas in axisymmetric contractions, elastic vortex growth and increased pressure drop co-existed, the planar contraction flow was Newtonian-like. Lip vortices were reported only for the planar contraction for supercritical flow rates, when the flow was unsteady.

The inexistence of lip vortices in the planar contraction for Boger fluids, and its presence for circular contractions remains to be explained, in spite of existing theoretical work (Binding, 1988; Xue et al, 1998a). Additionally, the experiments and numerical simulations of White and Baird (1986, 1988a, 1988b) have established the relevance of extensional stress growth near the contraction plane upon the vortex dynamics for the plane 4:1 and 8:1 contractions. For large circular contractions Rothstein and McKinley (2001) related the dominance of the lip or corner vortices to the competition between shear-induced and extension-induced normal stresses, later confirmed by the simulations of Oliveira et al (2007).

Regardless of the contraction, the growth of elasticity under conditions of negligible inertia inevitably leads to an instability, which may be chaotic at very large De or be preceded by periodic unsteady flow. This sequence of events has been seen as early as the late seventies by Cable and Boger (1978a, 1978b, 1979) and Nguyen and Boger (1979) and has been studied in detail by Lawler et al (1986), McKinley et al (1991) and Yesilata et al (1999).

The flows through abrupt contractions have recently been revisited in the context of microfluidics, in which high De can be easily attained due to the small characteristic dimensions, even with weakly elastic and viscous fluids as in the experiments of Rodd et al (2005) using dilute and semi-dilute aqueous solutions of poly(ethylene oxide). They observed the onset of divergent streamlines upstream of the recirculation at high De in addition to the elastic vortex growth. However, notice that in microfluidics, the flow is

often not truly planar (2D) due to the effects of the bounding walls (typically, aspect ratios are of the order of unity in the contraction region), which confer a 3D character to the flow.

4.2 Numerical simulations

Numerical investigations in contraction flows were also initiated in the late seventies, but soon problems of convergence arose leading to the development of robust and accurate numerical methods for predicting steady flows and in particular the elastic vortex growth seen in experiments. These extensive developments are well documented by Owens and Phillips (2002). Here, some of the most accurate and recent results in the 4:1 planar contraction flow for Oldroyd-B and PTT fluids are presented. The PTT fluid used here is the simplified version with $N_2=0$.

4.2.1 Oldroyd-B fluid

The flow geometry and the notation are shown in Figure 5. The Reynolds number ($Re \equiv \rho U_2 H_2 / \eta$) is set to zero by dropping out the convective term in the momentum equation. The Deborah number ($De \equiv \lambda U_2 / H_2$) is varied to investigate the effect of elasticity on the flow characteristics, and the solvent viscosity ratio considered was $\beta = \eta_s / \eta = 1/9$, the typical benchmark case.

Results for the Oldroyd-B fluid through the 4:1 sudden contraction were presented by Alves et al (2003b) who used the standard stress formulation and the HRS CUBISTA scheme together with very refined meshes with up to 169 392 computational cells, corresponding to more than one million degrees of freedom. The high accuracy of the results for $De \leq 2.5$, most of which have an uncertainty below 0.3%, indicates these values may be used as benchmark data (Alves et al, 2003b). The new predictions of Afonso et al (2011) for much higher Deborah numbers (up to $De = 100$), made possible by the log-conformation formulation, are also discussed here.

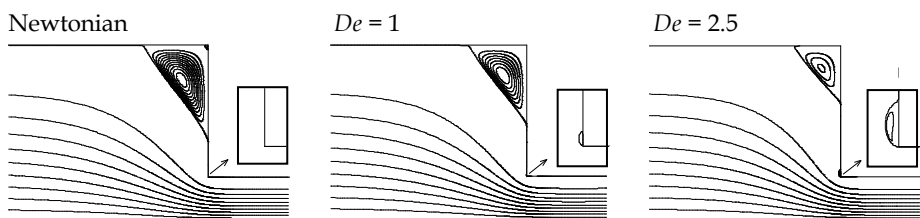


Fig. 6. Streamline plots for the flow of an Oldroyd-B fluid in a 4:1 plane sudden contraction for $De \leq 2.5$. Adapted from Alves et al (2003b).

The evolution of flow patterns with elasticity is shown in the streamline plots of Figure 6. The reduction of the corner vortex length with De for the Oldroyd-B fluid is clear as well as the appearance of a small lip vortex in the re-entrant corner as also happens with the UCM fluid (Alves et al, 2000). At $De = 2.5$ the lip vortex is still small, but stronger than at lower values of De . Although minute, this lip vortex is not a numerical artefact and has a finite

strength. Extrapolation of its size and strength to a zero mesh size from consecutively refined meshes confirms that assertion (see Alves et al, 2003b).

At approximately $De = 2.5$, local flow unsteadiness is detected near the re-entrant corner. For higher De , a different trend is found, as can be observed in Figure 7. Initially, as the De is increased further, the lip and corner vortex structures merge, as shown for $De = 5$. Simultaneously, the periodic unsteadiness grows with De leading to a loss of symmetry and eventually, alternate back-shedding of vorticity is observed from the upstream pulsating eddies at higher De . These features are accompanied by a frequency doubling mechanism deteriorating to a complex pattern and eventually to a chaotic regime as shown by the frequency spectra in Afonso et al (2011).

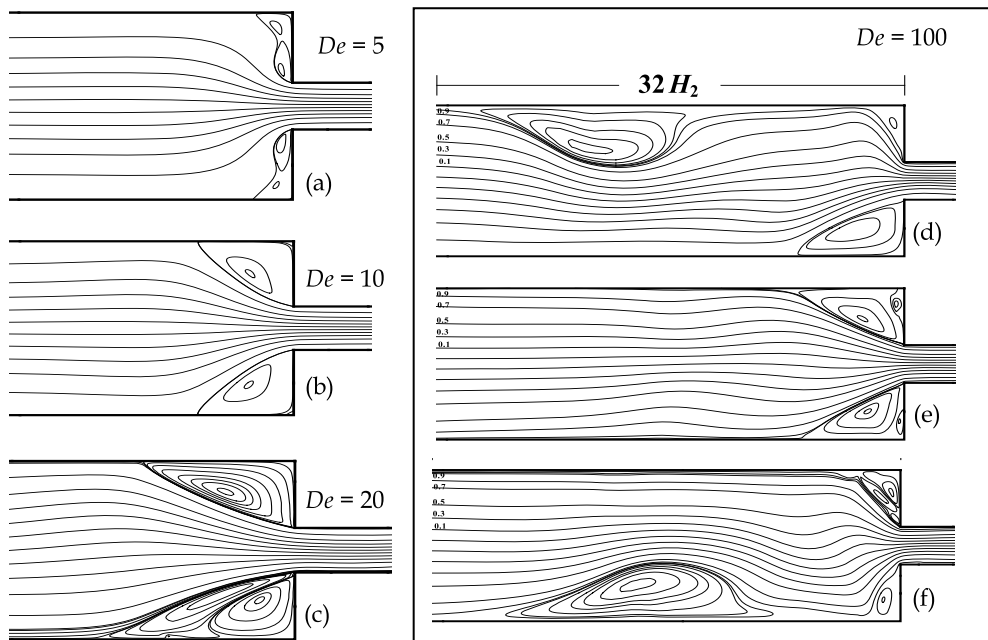


Fig. 7. Streamline plots for the flow of an Oldroyd-B fluid in a 4:1 plane sudden contraction for $De \geq 5$. Adapted from Afonso et al (2011).

The corresponding dimensionless corner vortex length ($X_R \equiv x_R/H_2$) is presented in Figure 8a, showing a non-monotonic variation with De . At low De the vortex size asymptotes to the Newtonian limit, as imposed by continuum mechanics. A semi-analytical investigation of creeping flow of Newtonian fluids by Rogerson and Yeow (1999) estimated the value $X_R = 1.5$ for a 4:1 planar contraction, which coincides with the numerical data of Alves et al (2003b) and Afonso et al (2011) in Figure 8a. Increasing De decreases the vortex size, in agreement with Aboubacar and Webster (2001). For $De \approx 4.5$, a minimum vortex length is attained and for larger values of De the vortex size increases significantly as well as its oscillation amplitude (as indicated by the error bars in Figure 8a).

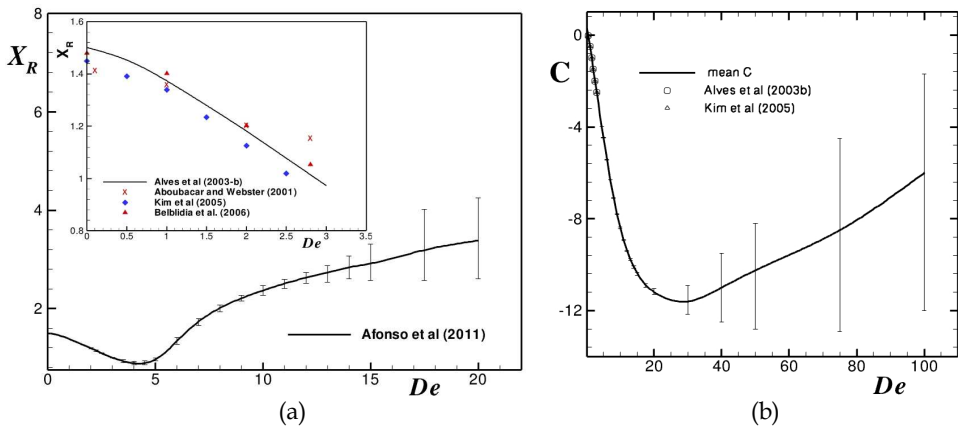


Fig. 8. Variation with De of the dimensionless vortex size (a) and Couette correction (b) for the flow of an Oldroyd-B fluid in a 4:1 planar sudden contraction. The error bars represent the amplitude of the oscillations. Adapted from Alves et al (2003b) and Afonso et al (2011).

Figure 8b plots the variation of the Couette correction (C) with De . C represents the dimensionless localized pressure loss across the contraction, and is defined as

$$C = \frac{\Delta p - (\Delta p_1)_{FD} - (\Delta p_2)_{FD}}{2\tau_w} \tag{49}$$

where $(\Delta p_1)_{FD}$ and $(\Delta p_2)_{FD}$ are the pressure drops associated with fully-developed flows in the inlet and outlet channels, respectively, and τ_w is the wall stress in the downstream channel under fully-developed conditions.

For low De , the Couette correction decreases with De and becomes negative (elastic pressure recovery), a behaviour which is contrary to the experimental evidence. Only for $De > 20$, an increase in C is observed, as seen in numerical studies with the PTT fluid (Alves et al 2003b). Once again, the error bars represent the oscillation amplitude, which is seen to increase significantly with De above the minimum C value attained.

4.2.2 PTT fluid

Numerical simulations with the PTT fluid model allow us to investigate the combined effects of shear-thinning of the viscometric viscosity and fluid elasticity via the first normal stress difference N_1 . From experimental data for contraction flow we know that the behaviour of such fluids is very different from the behaviour of Boger fluids. The results presented here are based on Alves et al (2003b), and were also obtained for creeping flow conditions, as in the previous section for the Oldroyd-B fluid. The PTT model corresponds to the simplified version ($\xi=0$) with a zero second-normal stress difference ($N_2=0$).

Since the PTT fluids have a bounded steady-state extensional viscosity, contrasting with the Oldroyd-B fluid, it was possible to obtain converged solutions up to De in excess of 100,

even using the standard stress formulation. This PTT model was also combined with a Newtonian solvent to define the same solvent viscosity ratio in the limit of very small rates of shear deformation, corresponding to $\beta = 1/9$. The PTT fluid is shear-thinning both in the shear viscosity as well as in the first-normal stress coefficient. The results presented here correspond to $\varepsilon = 0.25$, a typical value for both concentrated polymer solutions and polymer melts.

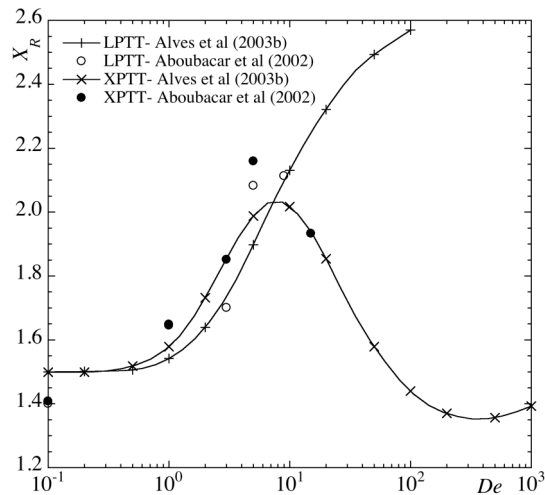


Fig. 9. Influence of elasticity on the recirculation length for the flow of PTT fluids in a 4:1 plane sudden contraction. LPTT: linear PTT; XPTT: exponential PTT. Adapted from Alves et al (2003b).

First, it is noted that the sensitivity of the PTT results to mesh fineness is lower than for the Oldroyd-B model and, in contrast to what happened with the Oldroyd-B fluid, the recirculation length (Figure 9) increases with De . This behaviour was expected given the experimental data available, where an intense vortex growth was seen for shear-thinning fluids. The recirculation length tends to stabilize at high De , and these predictions do not capture the elastic instabilities observed in experiments, but to assess whether this model is adequate to predict real flow conditions, where the vortex grows and then becomes unstable, simulations must be carried out using 3D meshes and time-dependent approaches with very small time-steps.

The evolution of the streamlines and the growth of the vortex with elasticity can be observed in Figure 10. The comparison with Figures 6-7 emphasises the differences between the behaviour of a shear-thinning fluid and a constant viscosity Boger fluid. At low De , the corner vortex grows towards the re-entrant corner while its size increases, but no lip vortex is observed. When the corner vortex occupies the whole contraction plane ($De = 2$) its shape changes from concave to convex and, as elasticity is further increased from $De \approx 2$ to $De \approx 10$, the vortex grows upstream even further. Simultaneously the eddy centre moves towards the re-entrant corner with the growth of elasticity. At high Deborah numbers the increase in X_R and Ψ_R becomes progressively less intense.

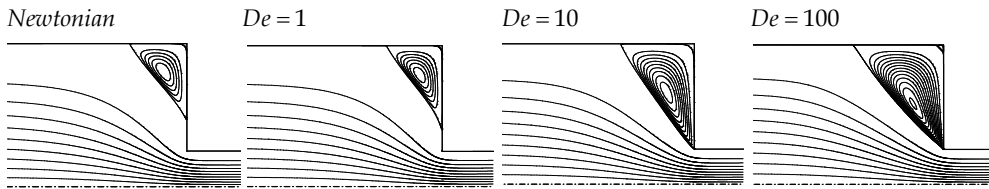


Fig. 10. Evolution of the flow patterns with De for a linear PTT fluid ($\varepsilon = 0.25$) in a 4:1 plane sudden contraction. Adapted from Alves et al (2003b).

The variation of the Couette correction for the linear PTT fluid is shown in Figure 11. C decreases with De until a minimum negative value is reached at $De \approx 20$, and then increases. Hence, the growth of C takes place only for $De > 20$ and therefore it is possible again to question the usefulness of this model to predict the enhanced pressure losses observed experimentally in sudden contraction flows. However, we should note the measurements of Nigen and Walters (2002) in a plane sudden contraction, which are not fully conclusive: in their Figure 13 there are negative values of C ($C = -1.37$) for a flow rate of 40 g/s with their Boger fluid 2 and shear-thinning syrup 2. It is possible that such negative values are due to the large experimental uncertainty, since their measurements in an axisymmetric sudden contraction with a short outlet pipe have shown a continuous drop in excess pressure drop ($C > 0$). More details of the predictions can be found in Alves et al (2003b).

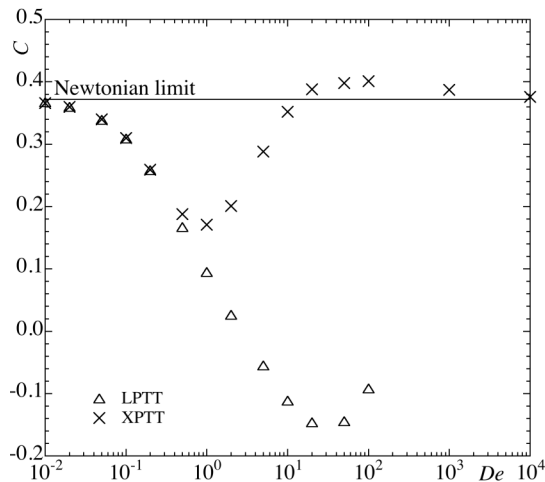


Fig. 11. Variation of the Couette correction with De for PTT fluids ($\varepsilon = 0.25$) in a 4:1 plane contraction flow. LPTT: linear PTT; XPTT: exponential PTT. Adapted from Alves et al (2003b).

The exponential stress coefficient in the PTT model (XPTT) substitutes the high strain plateau of the extensional viscosity by strain-thinning after the peak extensional viscosity. This affects the fluid dynamical behaviour of the PTT model since the fluid rheology tends to Newtonian-like at high shear and extensional deformation rates, as shown in Figures 9

and 11 which include results of predictions for the XPTT model. Our results for this fluid agree with the literature for X_R , Ψ_R and C , tending to the Newtonian values at very high De , as expected. For this model we could obtain iterative convergence at extremely high $De \approx 10\,000$, even using the standard stress formulation. Although more in line with experimental observations in terms of the variation of C with De , the computed values of C are still quite lower than those measured.

As a final comment, we remark that although part of the increase in C does correspond to a real increase in pressure drop, the major effect here is related to the normalization employed to define C where the pressure drop is scaled with the wall shear stress under fully-developed conditions in the downstream channel. Since this wall stress decreases significantly because of the shear-thinning behaviour of the PTT fluid (see Oliveira and Pinho, 1999c), the coefficient increases. This, and previous comments, pinpoint a crucial issue associated with constitutive equation modelling, as the current models are unable to predict correctly the enhanced entry pressure loss measured when elastic liquids flow through contractions. Most likely, models with increased internal energy dissipation are required for such purpose.

5. Acknowledgments

We are indebted to Fundação para a Ciência e a Tecnologia and FEDER for funding support over the years.

6. References

- Aboubacar M and Webster MF (2001). *J. Non-Newt. Fluid Mech.*, Vol. 98, pp. 83-106.
- Aboubacar M, Matallah H and Webster MF (2002). *J. Non-Newt. Fluid Mech.*, Vol. 103, pp. 65-103.
- Afonso AM, Oliveira PJ, Pinho FT and Alves MA (2009). *J. Non-Newt. Fluid Mech.*, Vol. 157, pp. 55-65.
- Afonso AM, Oliveira PJ, Pinho FT and Alves MA (2011). *J. Fluid Mech.*, Vol. 677, 272-304.
- Afonso AM, Pinho FT and Alves MA (2012). *J. Non-Newt. Fluid Mech.*, Vol. 167-168, pp. 30-37.
- Alves MA, Pinho FT and Oliveira PJ (2000). *J. Non-Newt. Fluid Mech.*, Vol. 93, pp. 287-314.
- Alves MA, Pinho FT and Oliveira PJ (2001a). *J. Non-Newt. Fluid Mech.*, Vol. 97, pp. 205-230.
- Alves MA, Pinho FT and Oliveira PJ (2001b). *J. Non-Newt. Fluid Mech.*, Vol. 101, pp. 55-76.
- Alves MA, Oliveira PJ and Pinho FT (2003a). *Int. J. Numer. Meth. Fluids*, Vol. 41, pp. 47-75.
- Alves MA, Oliveira PJ and Pinho FT (2003b). *J. Non-Newt. Fluid Mech.*, Vol. 110, pp. 45-75.
- Baliga RB and Patankar SV (1983). *Num. Heat Trans.*, Vol. 6, pp. 245-261.
- Bevis MJ, Darwish MS and Whiteman JR (1992). *J. Non-Newt. Fluid Mech.*, Vol. 45, pp. 311-337.
- Binding DM (1988). *J. Non-Newt. Fluid Mech.*, Vol. 27, 173-189.
- Bird RB, Armstrong RC and Hassager O (1987). *Dynamics of Polymeric Liquids. Volume 1: Fluid Mechanics*, John Wiley, New York.
- Boger DV, Hur DU and Binnington RJ (1986). *J. Non-Newt. Fluid Mech.*, Vol. 20, pp. 31-49.
- Boger DV (1987). *Annual Rev. of Fluid Mech.*, Vol. 19, 157-182.

- Cable PJ and Boger DV (1978a). *AIChE J*, Vol. 24, pp. 868-879.
- Cable PJ and Boger DV (1978b). *AIChE J*, Vol. 24, pp. 992-999.
- Cable PJ and Boger DV (1979). *AIChE J*, Vol. 25, pp. 152-159.
- Coates PJ, Armstrong RC and Brown RA (1992). *J. Non-Newt. Fluid Mech.*, Vol. 42, pp. 141-188.
- Crochet MJ, Davies AR and Walters K (1984). *Numerical Simulation of Non-Newtonian Flow*, Elsevier, Amsterdam.
- Darwish MS and Moukalled F (1994). *Num. Heat Transfer, Part B*, Vol. 26, pp. 79-96.
- Dean WR and Montagnon PE (1949). *Proc. Cambridge Philo. Soc.*, Vol. 45, pp. 389-394.
- Debbaut B, Marchal JM and Crochet MJ (1988). *J. Non-Newt. Fluid Mech.*, Vol. 29, pp. 119-146.
- Dou HS and Phan-Thien N (1999). *J. Non-Newt. Fluid Mech.*, Vol. 87, pp. 47-73.
- Evans RE and Walters K (1986). *J. Non-Newt. Fluid Mech.*, Vol. 20, pp. 11-29.
- Evans RE and Walters K (1989). *J. Non-Newt. Fluid Mech.*, Vol. 32, pp. 95-105.
- Fan Y, Tanner RI and Phan-Thien N (1999). *J. Non-Newt. Fluid Mech.*, Vol. 84, pp. 233-256.
- Fattal R and Kupferman R, (2004). *J. Non-Newt. Fluid Mech.* Vol. 123, pp. 281-285.
- Ferziger JH and Perić (2002). *Computational Methods for Fluid Dynamics*. Springer Verlag, 3rd edition, Berlin.
- Gaskell PH and Lau AKC (1988). *Int. J. Num. Meth. Fluids*, Vol. 8, pp. 617-641.
- Gervang B and Larsen PS (1991). *J. Non-Newt. Fluid Mech.*, Vol. 39, pp. 217-237.
- Hassager O (1988). *J. Non-Newt. Fluid Mech.*, Vol. 29, pp. 2-55.
- Hinch EJ (1993). *J. Non-Newt. Fluid Mech.*, Vol. 50, pp. 161-171.
- Hu HH and Joseph DD (1990). *J. Non-Newt. Fluid Mech.*, Vol. 37, pp. 347-377.
- Huang X, Phan-Thien N and Tanner RI (1996). *J. Non-Newt. Fluid Mech.*, Vol. 64, 71-92.
- Issa RI and Oliveira PJ (1994). *Computers and Fluids*, Vol. 23, pp. 347-372.
- Khosla PK and Rubin SG (1974). *Computers and Fluids*, Vol. 2, pp. 207-209.
- Lawler JV, Muller SJ, Brown RA and Armstrong RC (1986). *J. Non-Newt. Fluid Mech.*, Vol. 20, pp. 51-92.
- Leschziner MA (1980). *Comp. Methods Appl. Mech. Eng.*, Vol. 23, pp. 293-312.
- Leonard BP (1991). *Comp. Meth. Appl. Mech. Eng.*, Vol. 88, pp. 17-74.
- Mackenzie JA, Crumpton PI and Morton KW (1993). *J. Comput. Phys.*, Vol. 109, 1-15.
- Matallah H, Townsend P and Webster MF (1998). *J. Non-Newt. Fluid Mech.*, Vol. 75, pp. 139-166.
- Matos HM, Alves MA and Oliveira PJ (2009). *Num. Heat Transfer, Part B*, Vol. 56, pp. 351-371.
- McKinley G, Raiford WP, Brown RA and Armstrong RC (1991). *J. Fluid Mech.*, Vol. 223, pp. 411-456.
- Meijerink JA and Van Der Vorst HA (1977). *Math. of Comp.*, Vol. 31, pp. 148-162.
- Missirlis KA, Assimacopoulos D and Mitsoulis E (1998). *J. Non-Newt. Fluid Mech.*, Vol. 78, pp. 91-118.
- Moffatt HK (1964). *J. Fluid Mech.*, Vol. 18, pp. 1-18.
- Mompean G and Deville M (1997). *J. Non-Newt. Fluid Mech.*, Vol. 72, pp. 253-279.
- Morton KW and Paisley MF (1989). *J. Comput. Physics*, Vol. 80, pp. 168-203.
- Nguyen H and Boger DV (1979). *J. Non-Newt. Fluid Mech.*, Vol. 5, pp. 353-368.
- Nigen S and Walters K (2002). *J. Non-Newt. Fluid Mech.*, Vol. 102, pp. 343-359.

- Oliveira PJ (1992). Computer modelling of multidimensional multiphase flow and applications to T-junctions. PhD thesis, Imperial College, Univ. of London, UK.
- Oliveira PJ, Pinho FT and Pinto GA (1998). *J. Non-Newt. Fluid Mech.*, Vol. 79, pp. 1-43.
- Oliveira PJ and Pinho FT (1999a). *Num. Heat Transfer, Part B*, Vol. 35, pp. 295-315.
- Oliveira PJ and Pinho FT (1999b). *J. Non-Newt. Fluid Mech.*, Vol. 88, pp. 63-88.
- Oliveira PJ and Pinho FT (1999c). *J. Fluid Mech.*, Vol. 387, pp. 271-280.
- Oliveira PJ (2001). *Num. Heat Transfer, Part B*, 40, pp. 283-301.
- Oliveira PJ (2002). *Acta Mechanica*, Vol. 158, pp. 157-167.
- Oliveira MSN, Oliveira PJ, Pinho FT and Alves MA (2007). *J. Non-Newt. Fluid Mech.*, Vol. 147, pp. 92-108.
- Owens RG, Chauvière C and Phillips TN (2002). *J. Non-Newt. Fluid Mech.*, Vol. 108, pp. 49-71.
- Owens RG and Phillips TN (2002). *Computational Rheology*. Imperial College Press, London, UK.
- Patankar SV (1980). *Numerical Heat Transfer and Fluid Flow*. McGraw-Hill, New York.
- Patankar SV and Spalding DB (1972). *Int. J. Heat Mass Transfer*, Vol. 15, pp. 1787-1806.
- Perera MGN and Walters K (1977). *J. Non-Newt. Fluid Mech.*, Vol. 2, pp. 49-81.
- Phan-Thien N (1978). *J. Rheol.*, Vol. 22, pp. 259-283.
- Phan-Thien N and Dou H-S (1999). *Comput. Methods Appl. Mech. Eng.*, Vol. 180, pp. 243-266.
- Phan-Thien N and Tanner RI (1977). *J. Non-Newt. Fluid Mech.*, Vol. 2, pp. 353-365.
- Phillips TN and Williams AJ (1999). *J. Non-Newt. Fluid Mech.*, Vol. 86, pp. 215-246.
- Rajagopalan D, Armstrong RC and Brown RA (1990). *J. Non-Newt. Fluid Mech.*, Vol. 36, pp. 159-192.
- Rhie CM and Chow WL (1983). *AIAA J*, Vol. 21, pp. 1525-1532.
- Rodd LE, Scott TP, Boger DV, Cooper-White JJ, McKinley GH (2005). *J. Non-Newt Fluid Mech.* Vol. 129, pp. 1-22
- Rogerson MA and Yeow YL (1999). *J. Appl. Mech.- Trans ASME*, Vol. 66, pp. 940-944.
- Rothstein JP and McKinley GH (2001). *J. Non-Newt. Fluid Mech.*, Vol. 98, pp. 33-63.
- Sasmal, GP (1995). *J. Non-Newt. Fluid Mech.*, Vol. 56, pp. 15-47.
- Sato T and Richardson S (1994). *J. Non-Newt. Fluid Mech.*, Vol. 51, pp. 249- 275.
- Walters K and Webster M F (1982). *Phil. Trans. R. Soc. London A*, Vol. 308, pp. 199-218.
- Wapperom P and Webster MF (1998). *J. Non-Newt. Fluid Mech.*, Vol. 79, pp. 405-431.
- Wapperom P and Webster MF (1999). *Comput. Methods Appl. Mech. Eng.*, Vol. 180, pp. 281-304.
- White SA and Baird DG (1986). *J. Non-Newt. Fluid Mech.*, Vol. 20, pp. 93-101.
- White SA and Baird DG (1988a). *J. Non-Newt. Fluid Mech.*, Vol. 29, pp. 245-267.
- White SA and Baird DG (1988b). *J. Non-Newt. Fluid Mech.*, Vol. 30, pp. 47-71.
- Williamson CHK (1996). *Ann. Rev. Fluid Mech.*, Vol. 28, pp. 477-539.
- Van Doormal JP and Raithby GD (1984). *Num. Heat Transfer*, Vol. 7, pp. 147-163.
- Versteeg HK and Malalasekera W (2007). *An Introduction to Computational Fluid Dynamics: The Finite Volume Method*, 2nd Ed., Pearson Education Limited, Edinburgh, UK.
- Vinokur M (1989). *J. Comp. Physics*, Vol. 81, pp. 1-52.
- Xue S-C, Phan- Thien N and Tanner RI (1995). *J. Non-Newt. Fluid Mech.*, Vol. 59, pp. 191-213.

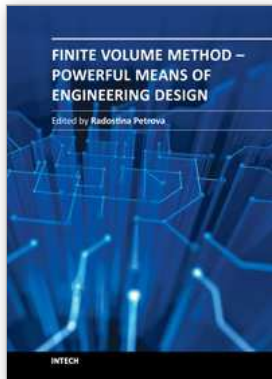
Xue S-C, Phan- Thien N and Tanner RI (1998a). *Rheol. Acta.*, Vol. 37, 158-169.

Xue S-C, Phan- Thien N and Tanner RI (1998b). *J. Non-Newt. Fluid Mech.*, Vol. 74, pp. 195-245.

Yesilata B, Öztekin A and Neti S (1999). *J. Non-Newt. Fluid Mech.*, Vol. 85, pp. 35-62.

Yoo JY and Na Y (1991). *J. Non-Newt. Fluid Mech.*, Vol. 39, pp. 89-106.

Zana E, Tiefenbruck F and Leal LG (1975). *Rheol. Acta*, Vol. 14, pp. 891-898.



Finite Volume Method - Powerful Means of Engineering Design

Edited by PhD. Radostina Petrova

ISBN 978-953-51-0445-2

Hard cover, 370 pages

Publisher InTech

Published online 28, March, 2012

Published in print edition March, 2012

We hope that among these chapters you will find a topic which will raise your interest and engage you to further investigate a problem and build on the presented work. This book could serve either as a textbook or as a practical guide. It includes a wide variety of concepts in FVM, result of the efforts of scientists from all over the world. However, just to help you, all book chapters are systemized in three general groups: New techniques and algorithms in FVM; Solution of particular problems through FVM and Application of FVM in medicine and engineering. This book is for everyone who wants to grow, to improve and to investigate.

How to reference

In order to correctly reference this scholarly work, feel free to copy and paste the following:

A.M. Afonso, M.S.N. Oliveira, P.J. Oliveira, M.A. Alves and F.T. Pinho (2012). The Finite Volume Method in Computational Rheology, Finite Volume Method - Powerful Means of Engineering Design, PhD. Radostina Petrova (Ed.), ISBN: 978-953-51-0445-2, InTech, Available from: <http://www.intechopen.com/books/finite-volume-method-powerful-means-of-engineering-design/the-finite-volume-method-in-computational-rheology>

INTECH

open science | open minds

InTech Europe

University Campus STeP Ri
Slavka Krautzeka 83/A
51000 Rijeka, Croatia
Phone: +385 (51) 770 447
Fax: +385 (51) 686 166
www.intechopen.com

InTech China

Unit 405, Office Block, Hotel Equatorial Shanghai
No.65, Yan An Road (West), Shanghai, 200040, China
中国上海市延安西路65号上海国际贵都大饭店办公楼405单元
Phone: +86-21-62489820
Fax: +86-21-62489821